University of Zawia Journal of Engineering Sciences and Technology (UZJEST)
Volume 4, Issue 2, (2026), pp 210-225, ISSN 3006-2764

CFD Analysis of NACA 4412 Airfoil Aerodynamics in Ground Effect

Elhassen Omer [*1], Zainab Ahmed [2]

[1]Mechanical Engineering Department, Faculty of Engineering, Zawia University, Zawia, Libya

[2]Aeronautical Engineering Department, Faculty of Engineering, Tripoli University, Tripoli, Libya

*Corresponding author email: e.amr@zu.edu.ly

Received: 13-09-2026 | Accepted: 08-11-2026 | Available online: 14-11-2026 | DOI:10.26629/uzjest.2026.16

ABSTRACT

Ground effect is an aerodynamic phenomenon characterized by the flow field modifications that occur when an airfoil operates in close proximity to a solid surface. In this paper, the performance of the NACA 4412 airfoil, commonly utilized in general aviation, is analysed at ground proximity effect conditions using ANSYS Fluent. The numerical analysis was evaluated at a Reynolds number of Re =3.5×10^5 by solving the steady, incompressible RANS equations coupled with the SST k-ω turbulence model. The study investigates the influence of normalized ground clearances ranging from 0.1 to 13, across various angles of attack from -3° to 18° on the aerodynamic characteristics. Quantitative evaluations of lift coefficient, drag coefficient and lift to drag ratio are presented, complemented by pressure and velocity contour visualizations. The results indicate that ground proximity is highly beneficial for augmenting lift; specifically, the airfoil experiences a progressive lift enhancement and a concurrent drag reduction as the ride height decreases. The aerodynamic efficiency increases until reaching its maximum at angle of attack (α) = 6°, after which it declines with further increases in angle of attack due to the onset of flow separation on the upper surface. Overall, the ground presence exerts significant effects on the airfoil aerodynamics; for instance, at α = 6°, reducing the ride height from 3.0C to 0.1C results in a 15.7% increase in lift coefficient, a 17.2% reduction in drag coefficient and a 33.8% improvement in the lift to drag ratio.

Keywords: Ground effect, Lift, Drag, Turbulent flow, ANSYS FLUENT

دراسة عددية للديناميكا الهوائية للجنيح NACA4412 تحت تأثير الأرض

الحسن عمرو [1] زينب أحمد [2]

[1] قسم الهندسة الميكانيكية، كلية الهندسة، جامعة الزاوية، الزاوية، ليبيا.

[2] قسم هندسة الطيران، كلية الهندسة، جامعة طرابلس، طرابلس، ليبيا.

ملخـــــص البحـــــث

تميز الطائرات ذات الأجنحة الثابتة عادةً بمرحلتي إقلاع وهبوط تكونان على ارتفاع منخفض ويؤدي هذا النوع من الطيران المنخفض إلى ظاهرة تُعرف باسم تأثير الأرض، والتي يتحسّن فيها الأداء الديناميكي الهوائي للطائرة أثناء طيرانها. وقد ركزت العديد من الدراسات على هذه الظاهرة، وصُممت بعض الطائرات خصيصًا للاستفادة منها. في هذه الدراسة تمت محاكاة وتحليل التدفق على

"Articles published in *Univ Zawia J Eng Sci Technol* are licensed under a Creative Commons Attribution-NonCommercial 4.0 International License."

مقطع NACA4412 ثنائي الأبعاد تحت تأثير الأرض على خصائص الديناميكيا الهوائية عند رقم رينولدز ×1053.5 وذلك باستخدام برنامج ANSYS Fluent عبر حل معادلات RANS المستقرة وغير القابلة للانضغاط مع دمج نموذج اضطراب SST k−ω. واستقصت الدراسة تأثير الارتفاعات الأرضية والتي تراوحت من 0.1 إلى 13 من طول الوتر عبر زوايا هجوم مختلفة تراوحت بين− 3°و 18°على الخصائص الديناميكية الهوائية لمقطع الجناح. وتم تقديم التقييمات الكمية لمعامل الرفع، ومعامل السحب، الهوائية ونسبة الرفع إلى السحب، مدعمة برسم خطوط لتوزيعات الضغط والسرعة. وتُشير النتائج إلى أن القرب من الأرض مفيد للغاية في تعزيز قوة الرفع؛ حيث شهد مقطع الجناح زيادة تدريجية في الرفع وانخفاضًا متزامنًا في السحب كلما انخفض الارتفاع عن الأرض، مما يؤكد حدوث ظاهرة تأثير الأرض. وتزداد الكفاءة الديناميكية الهوائية حتى تصل إلى قيمتها العظمى عند زاوية هجوم α = 6° ثم تنخفض مع أي زيادة إضافية في زاوية الهجوم نتيجة لبداية انفصال التدفق على السطح العلوي لمقطع الجناح. وبشكل عام، تظهر النتائج أن وجود الأرض يمارس تأثيرات جوهرية على الخصائص الديناميكية الهوائية لمقطع الجناح؛ حيث وُجد أنه في حالة زاوية الهجوم = α 6°، وعندما يتغير الارتفاع النسبي من الأرض للجنيح من 3 إلى 0.1، ازدادت قيمة معامل الرفع بنسبة تصل إلى 15.7%، وانخفضت قيمة معامل السحب بنسبة تصل إلى 17.2%، بينما ارتفعت نسبة الرفع إلى السحب بمقدار 33.8% .

الكلمات الدالة: تأثير الأرض، قوة الرفع، قوة السحب، التدفق المضطرب، ANSYS FLUENT.

1. Introduction

The aerodynamic characteristics of an airfoil or a wing operating in ground proximity are of significant interest due to their diverse applications, including aircraft take-off and landing sequences, high-speed marine vessels, and high-performance racing cars. When a wing operates at small angles of attack close to the ground, lift increases due to the formation of a high-pressure air cushion beneath the lower surface, while induced drag decreases due to the reduction in downwash velocity. Consequently, the lift-to-drag ratio is substantially enhanced [1]. Ground effect occurs when the proximity to the surface interferes with the airflow patterns around the aircraft, typically manifesting within a distance of one wingspan above the ground. During landing, if the approach airspeed is excessively high, this phenomenon causes the aircraft to float along the runway, thereby delaying touchdown. Accordingly, numerous studies have investigated and characterized ground effect on wings and airfoils utilizing analytical, numerical, and experimental methodologies.

Several researchers [2–5] have numerically investigated the aerodynamic characteristics of various airfoils in ground effect, focusing on the influences of the Reynolds number and ride height. For instance, an inverted single-element CLARK-Y airfoil was numerically evaluated under both unbounded and ground effect configurations [2]. The findings revealed that the lift coefficient C_L increased proportionally with the angle of attack up to $\alpha = 10^o$, beyond which stall occurred. Furthermore, ground proximity generally enhanced C_L, except at extremely low clearances of $h/c < 0.1$, where a force reduction phenomenon was observed.

Additionally, the aerodynamic efficiency of the bio-inspired corrugated and cambered airfoils in ground effect was investigated numerically [3], and their study focused on the effects of flapping motion on the flow field around two subsonic airfoils in close proximity to a ground boundary. Their findings indicated a direct relationship between the airfoil's aerodynamic performance and the ground effect. Similarly, the influence of a flap on a two-dimensional NACA 4412 airfoil in a viscous ground-effect flow was investigated [4]. Their study evaluated the aerodynamic forces, presented the combined effects of the Reynolds number, and ground clearance. The findings indicated that the aerodynamic performance underground effect can be further enhanced either by introducing flaps to the airfoil configuration or by

adjusting its operational angle of attack. Furthermore, a CFD analysis focusing on the flow field around a complete wing-in-ground (WIG) effect craft flying over both wavy and flat ground topologies was conducted using ANSYS Fluent [5]. Utilizing the Spalart–Allmaras turbulence model, the investigation varied the angle of attack within the range of 3° to 9°. The simulation results demonstrated that the cycle-averaged aerodynamic coefficients obtained over wavy ground vary with flight height in the same pattern as those recorded over flat ground.

Experimentally, the aerodynamic and flow field characteristics of a NACA 0012 airfoil subjected to both stationary ground and moving ground effects were investigated in the same wind tunnel flow facility [6-8]. Their findings indicated that the surface pressure coefficient C_p increased on the airfoil's lower surface as the stationary ground was approached, consequently enhancing C_L. Furthermore, the flow accelerated over the upper surface due to flow diversion from the lower surface, particularly at higher angles of attack, which resulted in a thicker wake and a corresponding increase in drag. Additionally, they concluded that for the stationary ground configuration, the development of a longitudinal boundary layer on the ground surface narrowed the flow passage beneath the airfoil. This boundary layer growth decelerated the flow underneath, thereby generating a higher $\mathbf{C_L}$ compared to the moving ground condition. Experimental studies [9–13] were carried out to investigate the aerodynamic performance of various airfoils, such as the E423, S8036, and NACA 0012, under the influence of ground proximity. These investigations evaluated at different Reynolds numbers, with the normalized ground clearance h/C varying from 0.1 to 1.0. Aerodynamic forces, surface pressure distributions, ground plane pressures, and lift and drag curves were meticulously recorded and analyzed. The C_L results revealed that at extremely low ground clearances ($h/C < 0.5$), viscous effects became highly predominant, which hindered the generation of sufficient aerodynamic forces; however, these viscous constraints diminished as the ride height increased slightly. Furthermore, the results demonstrated a reduction in drag within the h/C range of 0.2 to 0.5, while concurrently augmenting lift, thereby significantly improving the overall aerodynamic efficiency.

In the present study, a NACA 4412 airfoil operating in ground proximity was simulated numerically. The steady-state RANS equations were solved using the commercial CFD code ANSYS Fluent. The simulations were performed at a Reynolds number of $\mathbf{Re} = 3.5\times10^5$ across a wide range of angles of attack and ride heights. The resulting aerodynamic performance parameters—including lift, drag, and the lift-to-drag ratio were systematically plotted and analysed.

2. Methodology

In the present study, the high fidelity ANSYS Fluent was used to solve the flow field governing equations, describing the flow over airfoil in a rectangular computational domain to compute the aerodynamic characteristics of wing in ground configurations.

2.1 Airfoil and Computational Domain

This study aims to investigate the effects of ground proximity on the aerodynamic parameters of an airfoil in ground effect. For this purpose, the aerodynamic profile was modeled using a NACA 4412 airfoil section, with its coordinates generated based on the specific NACA series designation. The chord length was set to 1 m. A two-dimensional rectangular computational domain was created; the distances from the airfoil to the domain's top, inlet, and outlet boundaries were defined as 13C, 13C, and 26C, respectively. The clearance between the airfoil and the ground plane was adjusted based on the specific normalized ride height tested. The computational domain and its corresponding boundary conditions are illustrated in Fig. 1.

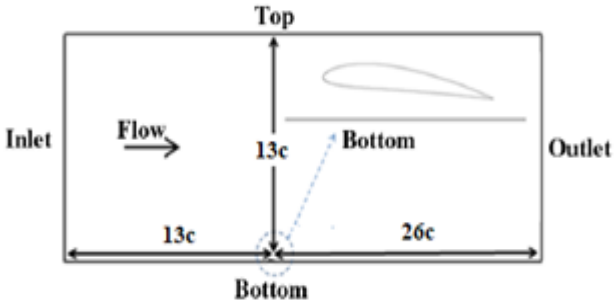


Figure 1. The computational domain and boundary conditions.

2.2 Mathematical Modelling and Data Analysis

The governing equations, based on the fundamental concepts of mass and momentum conservation, were employed to resolve the flow field behaviour over the airfoil in ground effect. The fluid flow was assumed to be steady, incompressible, two-dimensional (2D), and turbulent. The continuity and Reynolds-Averaged Navier-Stokes (RANS) equations are expressed as follows [14-16]:

$$\frac{\partial}{\partial x_i}\ (\rho u_i) = 0 \tag{1}$$

$$\frac{\partial}{\partial x_j}\left(\rho u_j u_i\right) = -\frac{\partial P}{\partial x_i} + \frac{\partial}{\partial x_j}\left[\mu\left(\frac{\partial u_i}{\partial x_j} + \frac{\partial u_j}{\partial x_i}\right)\right] + \mu_t \frac{\partial}{\partial x_j}\left(\frac{\partial u_i}{\partial x_j} + \frac{\partial u_j}{\partial x_i}\right) \tag{2}$$

Where:

p	pressure, (Pa).
u, u'	velocity component and velocity fluctuations, (m/s).
ρ	air density, (kg/m^3).
μ, μ_t	dynamic and turbulent viscosity, (kg/ms).

The Shear-Stress Transport (SST) k–ω turbulence model was employed for closure. This model was selected based on established literature for similar aerodynamic computations and its proven capability in capturing flow separation over airfoils and ground-bound walls. The transport equations for the turbulence kinetic energy k and the specific dissipation rate ω are expressed as follows [17]:

$$\frac{\partial \rho u_j k}{\partial x_j} = P - \beta^* \rho \omega k + \frac{\partial}{\partial x_j}\left[\left(\mu + \sigma_k \mu_t\right)\frac{\partial k}{\partial x_j}\right] \tag{3}$$

$$\frac{\partial \rho u_j \omega}{\partial x_j} = \frac{\alpha}{v_t} P - \beta \rho \omega^2 + \frac{\partial}{\partial x_j}\left[\left(\mu + \sigma_\omega \mu_t\right)\frac{\partial \omega}{\partial x_j}\right] + 2(1 - F_1)\frac{\rho \sigma \omega^2}{\omega}\frac{\partial k}{\partial x_j}\frac{\partial \omega}{\partial x_j} \tag{4}$$

Where:

k Turbulent kinetic energy, (J kg^{-1}),

ω Specific dissipation rate, (m^2/s), and

$$S = \sqrt{2 S_{ij} S_{ji}} \tag{5}$$

The expression for the mean strain rate tensor S_{ij} and the expression for the production term P are:

$$S_{ij} = \frac{1}{2}\left(\frac{\partial \overline{u_i}}{\partial x_j} + \frac{\partial \overline{u_j}}{\partial x_i}\right) \tag{6}$$

$$P = \min\left[\tau_{ij}\frac{\partial u_i}{\partial x_j}, 10\beta^*\ \rho\omega k\right] \tag{7}$$

The SST k – ω ANSYS formulation, expresses the turbulent viscosity and blending functions F_1 and F_2 defined by the relations [18]:

$$\mu_t = \frac{\rho a_1 k}{max[a_1\omega, SF_2]} \quad (8)$$

$$F_1 = \tanh\left(\min\left[\max\left[\frac{\sqrt{k}}{\beta^*\omega d}, \frac{500v}{d^2\omega}\right], \frac{4\rho\sigma_{\omega 2}k}{CD_{k\omega}d^2}\right]^4\right) \quad (9)$$

$$F_2 = \tanh\left(\max\left[2\frac{\sqrt{k}}{\beta^*\omega d}, \frac{500v}{d^2\omega}\right]^2\right) \quad (10)$$

$$CD_{k\omega} = max\left[2\rho\sigma_{\omega 2}\ \frac{1}{\omega}\ \frac{\partial k}{\partial x_j}\ \frac{\partial \omega}{\partial x_j}, 10^{-10}\right] \quad (11)$$

The model constants and parameters used in the model [19]:

$\alpha_1 = \frac{5}{9}$ $\alpha_2 = 0.44$ $\sigma_{k1} = 0.85$ $\sigma_{\omega 1} = 0.500$ $\beta_1 = 0.075$

$\sigma_{k2} = 1.00$ $\sigma_{\omega 2} = 0.856$ β_2 0.0828 $\beta^* = 0.09$ $k = 0.41$ $\alpha_1 = 0.31$

To evaluate and compare the aerodynamic characteristics across the various ride heights, the lift, drag, and pressure coefficients are defined, respectively, as follows [20]:

$$C_L = \frac{L}{\frac{1}{2}\rho u_\infty^2\, C} \quad (12)$$

$$C_D = \frac{D}{\frac{1}{2}\rho u_\infty^2\, C} \quad (13)$$

$$C_p = \frac{P_i - P_\infty}{\frac{1}{2}\rho u_\infty^2} \quad (14)$$

Where:

C is the airfoil chord length (m),

L is the lift force (N),

D is the drag force (N),

u_∞ is the free stream velocity (m/s),

ρ is the air density, (kg/m^3),

p_i is the pressure at a given point, (Pa), and

p_∞ is the free stream pressure, unaltered by the interaction with the airfoil. (Pa).

The lift-to-drag ratio **(**L/D**),** also referred to as aerodynamic efficiency or glide ratio, serves as a quantitative measure of an aerodynamic body's effectiveness in generating lift relative to the magnitude of drag it produces [21].

$$E = L/D \quad (15)$$

2.3 Boundary Conditions

To ensure an accurate numerical solution, the boundary conditions must be meticulously specified. The established computational domain and its boundaries are illustrated in Fig. 1. Air with constant physical properties at room temperature was employed as the working fluid. Accordingly, the following boundary conditions were adopted [22]:

1. The upstream boundary was modeled as a velocity inlet, with the inflow velocity set to correspond to a Reynolds number of Re = 3.5 ×10^5.

2. The downstream boundary was modeled as a pressure outlet, with the gauge pressure set to zero Pascal.
3. A no-slip wall condition was enforced on the airfoil surface, prescribing zero relative velocity.
4. The top boundary of the computational domain was defined as a pressure far-field, which serves as a non-reflecting boundary condition to simulate free-stream conditions at infinity. The corresponding Mach number and static thermodynamic variables were specified accordingly.
5. The bottom boundary representing the ground was modeled as a moving wall with a non-slip condition. The translational velocity of the ground was set equal to the free stream velocity to prevent artificial boundary layer growth and eliminate non-physical velocity gradients near the wall.

2.4 Numerical Procedure

The commercial CFD software, ANSYS Fluent 2025 R1, was employed to solve the RANS and SST k–ω equations using a cell-centred finite volume discretization method. For the spatial discretization of the computational domain, an unstructured mesh with triangular elements was generated due to its flexibility in handling complex geometries. To optimize the flow analysis, the computational domain was divided into two distinct subdomains**.** A highly refined mesh was prescribed near the airfoil surfaces, whereas the outer regions were coarsely meshed to minimize the total node count and reduce computational overhead. To properly resolve the boundary layer and ensure accurate computation of the aerodynamic coefficients, an inflation layer was applied over the airfoil surface, featuring 50 layers with a growth rate of 1.15. The first grid cell height from the wall was set to 1×10^{-5}m, securing a dimensionless wall distance of ($y^+ < 1.5$) [23]. Furthermore, critical mesh quality metrics; including aspect ratio, orthogonal quality, and skewness; strictly adhered to the recommended thresholds specified by ANSYS Fluent. The final mesh configuration used in the simulations is illustrated in Fig. 2.

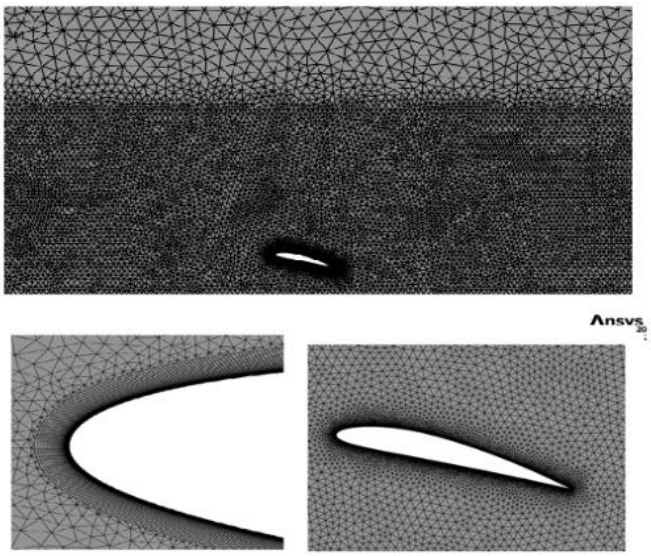


Figure 2. The computational domain meshing.

The governing flow equations were solved using a pressure-based solver with double precision. The COUPLED algorithm was employed for pressure-velocity coupling. Spatial discretization was achieved using a second-order pressure scheme for pressure interpolation, while second-order upwind schemes were selected for the momentum, turbulence kinetic energy, and specific dissipation rate equations. Gradient evaluation was performed using the least-squares cell-based formulation. A residual threshold of (10^{-6}) was established as the convergence criterion for both the flow equations and turbulence quantities, beyond which no significant variations in the aerodynamic coefficients were observed. To

accelerate convergence, the flow field was initialized using the hybrid initialization technique, which executes boundary interpolation methods to solve Laplace's equations, thereby providing a smooth and mathematically sound initial guess tailored to complex domain geometries.

3. Grid Independence Test and Code Validation

An increased number of nodes is generally required to enhance numerical accuracy; however, grid refinement inherently escalates the computational overhead and memory requirements. To assess grid sensitivity, multiple mesh configurations were examined based on the lift coefficient C_L of the airfoil at $\alpha = 15°$ and $Re = 6\times10^6$. Grid independence was established when the relative variation in the lift coefficient between successive meshes was below 1%, provided that the wall-distance criterion of ($y^+ < 1.5$) was strictly maintained. The grid independence test results are summarized in Table 1. Based on these criteria, Mesh C was selected for all subsequent simulations in this study.

Table 1. Grid independence test and mesh quality parameters

Mesh	Number of Nodes	C_L	Orthogonal Quality	Average Skewness	y+
A	188944	0.96577	0.96046	5.88E-02	5.18941
B	430533	1.630937	0.96527	6.13E-02	0.60510
C	**684175**	**1.636139**	**0.96566**	**5.94E-02**	**0.10410**
D	848318	1.640253	0.96643	6.10E-02	0.03728

The predictive capability of the CFD simulation was assessed by computing the lift coefficient of the flow over the NACA 4412 airfoil. The simulation was carried out for an angle of attack range of $\alpha = -6° \sim 20°$ and $Re = 6\times10^6$ within an unbounded flow field. The lift curves from the present study, the numerical data of [24], and the NASA experimental data [25] were compared and plotted in Fig. 3.

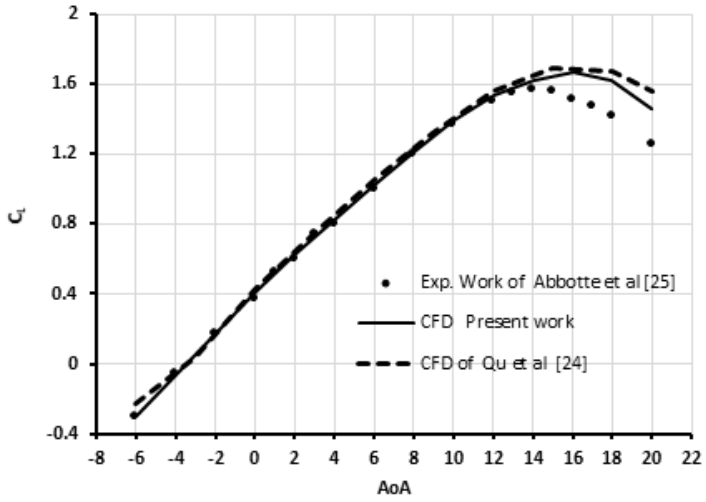


Figure 3. Validation of the current study with numerical and experiments results.

Excellent agreement is observed between the numerical and experimental results within the linear region of the C_L curve, indicating fully attached flow in the range of $\alpha = -4° \sim 12°$. At higher angles of attack, the slope of the C_L curve begins to decline. This behaviour reflects a known limitation in CFD calculations where flow separation prediction is typically delayed. This delay is attributed to the employment of the SST *k*-ω turbulence model, which assumes a fully turbulent boundary layer and consequently over predicts the turbulent eddy viscosity.

4. Results and Discussion

The NACA 4412 airfoil profile was selected for the 2D WIG problem. The flow was investigated at different ride heights (h/C) of 0.1, 0.25, 0.5, 1.0, 3.0, and 6.0, as well as (h/c = 13.0), which represents the unbounded case. For all cases, angles of attack ranging from-3° to 18 were tested at a fixed Reynolds number of $Re = 3.5\times10^5$.

The lift coefficient curves of the NACA 4412 airfoil at various ride heights were recorded and plotted for the upper surface ($C_{L,US}$) and lower surface ($C_{L,LS}$). For all angles of attack, the upper surface of the airfoil generates positive lift, which decreases with decreasing ride height. Higher angles of attack result in a more pronounced decrease in upper surface lift. The lift coefficient curve for the upper surface is shown in Fig. 4. Conversely, the lower surface produces positive lift at positive angles of attack, which increases as the ride height decreases. However, at negative angles of attack, the lower surface produces negative lift, which decreases in magnitude as the ride height is reduced, as shown in Fig. 5.

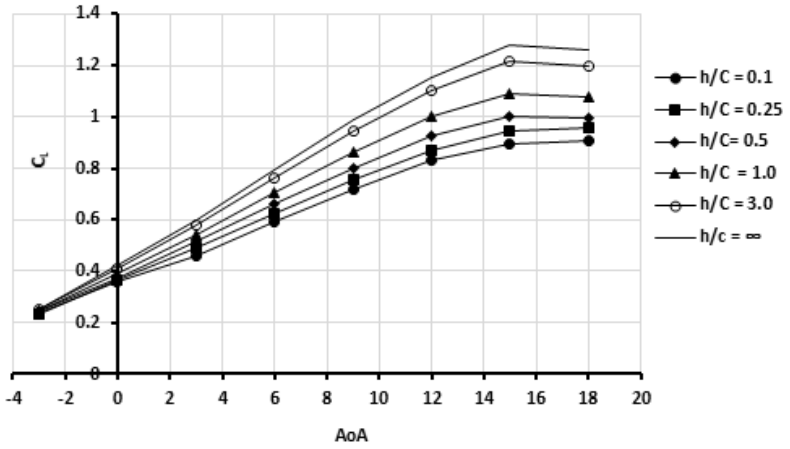


Figure 4. Upper side lift for the NACA 4412 airfoil at various ride heights.

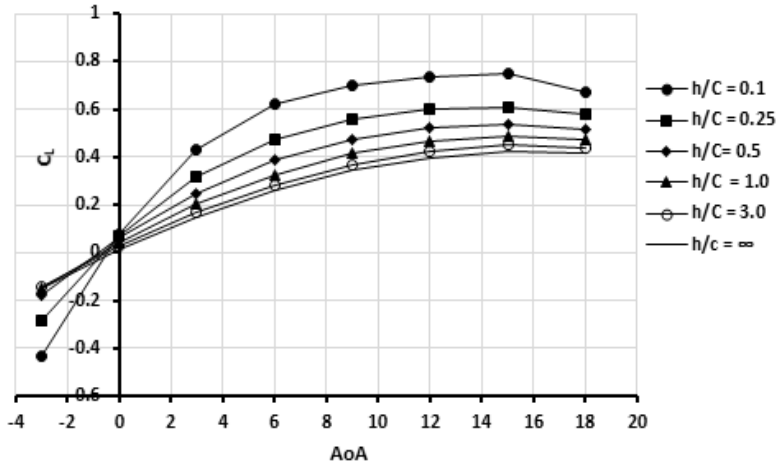


Figure 5. Lower side lift for the NACA 4412 airfoil at various ride heights.

Fig. 6 shows the total lift coefficient curve, which is determined by summing the upper and lower surface coefficients. In unbounded flow, the curve exhibits a linear portion within the range of $\alpha = 0°$ to 10°; in contrast, at different ride heights, the curves display a convex behavior in this range. As the ride height

decreases, the curvature of this convex portion becomes more pronounced, and the angles of attack corresponding to the intersection points shift to higher values. Outside the region bounded by these intersection points, lift decreases with decreasing ride height. However, within the region between the two intersections points lift increases with decreasing ride height. These results highlight the significance of the ground effect; for instance, at $\alpha = 6°$, the lift coefficient increases by 15.7% when (h/C) decreases from 3.0 to 0.1.

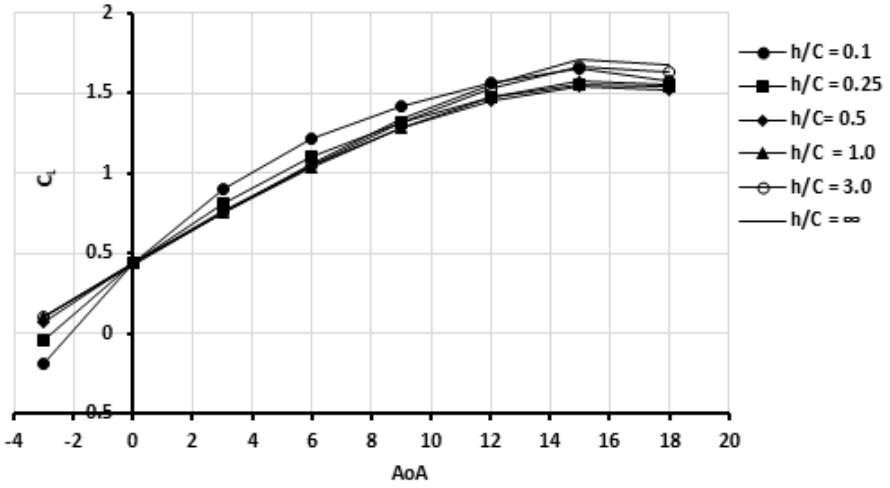


Figure 6. Total lift for the NACA 4412 airfoil at various ride heights.

Fig. 7 illustrates the variation in lift coefficients with ride height at $\alpha = 6°$. In unbounded flow (h/C = 13.0), $C_{L,US}$ is much greater than $CL_{,LS}$. As the ride height decreases, $C_{L,US}$ gradually declines, whereas $C_{L,LS}$ steadily increases. This increase in $C_{L,LS}$ accelerates at lower ride heights, leading to $C_{L,LS}$ surpassing $C_{L,US}$ at very low clearances.

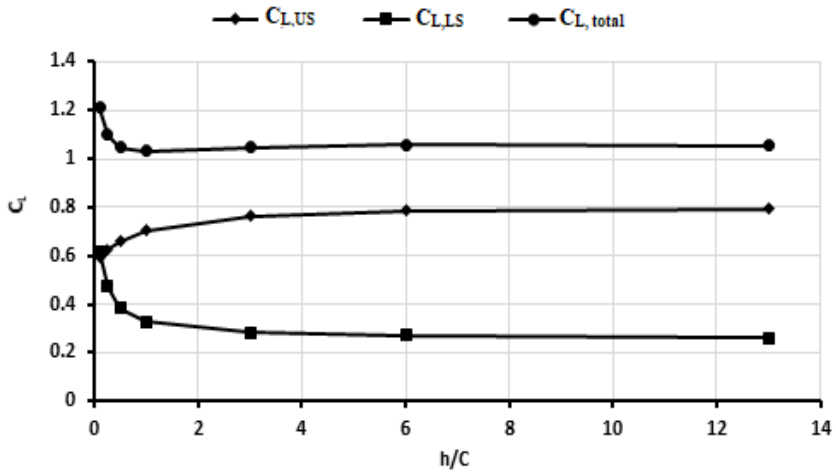


Figure 7. Variations of lift versus ride heights at $\alpha = 6^0$.

Fig. 8 illustrates the total drag coefficient curves at various ride heights compared to the unbounded flow condition. The drag magnitude increases as the ride height of the airfoil from the ground increases. For instance, at $\alpha = 6°$, the results show that the drag coefficient decreases by 17.2% when (h/C) is reduced from 3.0 to 0.1. Furthermore, it is noted that at higher angles of attack $\alpha > 9°$, the drag increases drastically due to flow separation at the trailing edge of the upper surface.

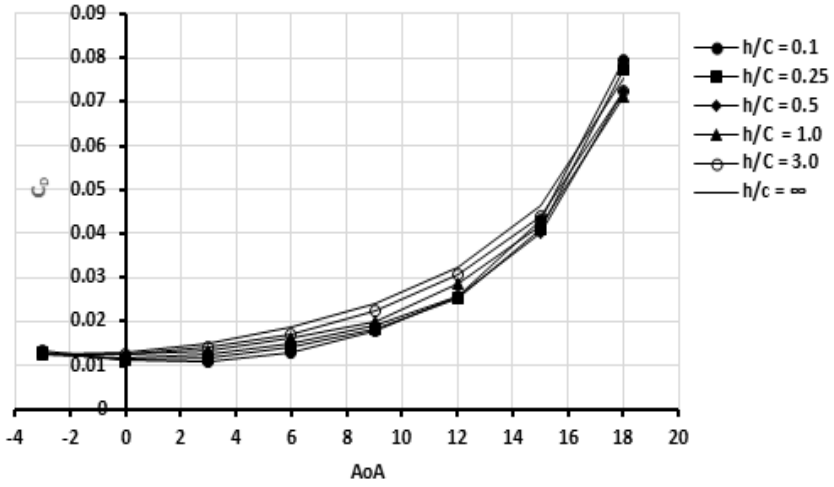


Figure 8. Drag for the NACA 4412 airfoil at various ride heights.

The resulting lift-to-drag (L/D) ratios are plotted in Fig. 9. For all ride heights, the (L/D) ratio increases progressively until reaching its maximum value at $\alpha = 6°$, after which it declines with further increases in angle of attack. This trend is attributed to the onset of flow separation on the upper surface near the trailing edge at high angles of attack. Consequently, at $\alpha = 6°$, the simultaneous increase in C_L and decrease in C_D significantly enhances the **(**L/D) ratio by 33.8% as (h/C) reduced from 3.0 to 0.1.

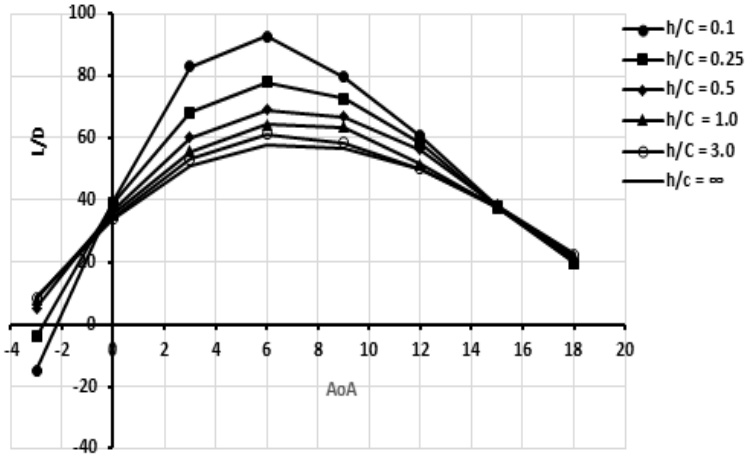


Figure 9. Lift-to-Drag ratio for the NACA 4412 airfoil at various ride heights.

The dependence of CL and C_D on (h/C) is plotted for various angles of attack within the range of $0° \leq \alpha \leq 12°$. For the C_L curves shown in Fig. 10, the maximum values occur at the lowest (h/C) and gradually decrease with increasing ride height. The drag coefficient C_D profiles are presented in Fig. 11. At fixed angles of attack within the range of $0° \leq \alpha \leq 9°$, C_D increases slightly with increasing (h/C). However, at $\alpha = 12°$, C_D exhibits a local maximum at the lowest (h/C) of 0.1, decreases until (h/C) = 0.5, and subsequently increases gradually at higher ride heights. Fig. 12 illustrates the aerodynamic performance by presenting the lift-to-drag ratio as a function of ride height for different angles of attack. Comparison of these (L/D) ratios indicates that the optimum performance, with a maximum (L/D) of 92, is obtained at $\alpha = 6°$ and (h/c)= 0.1. Generally, the lowest lift-to-drag ratio across the investigated ride heights occurs at $\alpha = 0°$.

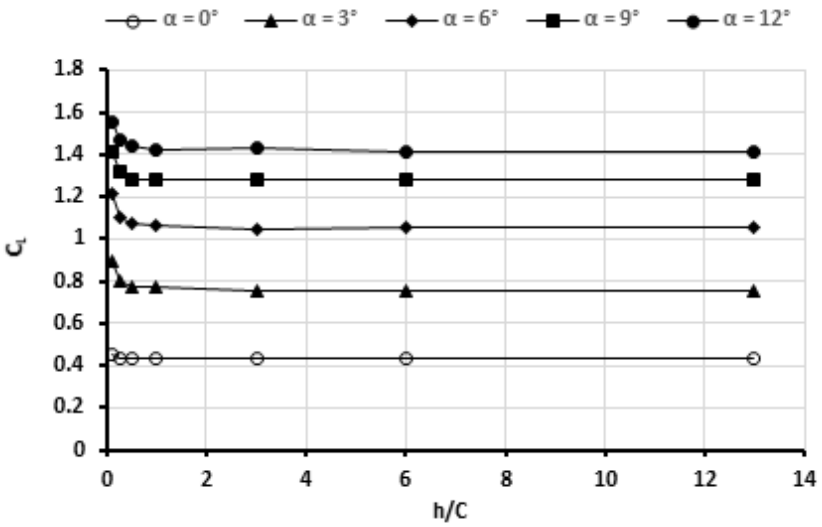


Figure 10. Lift coefficient variation with ride height at various angles of attack.

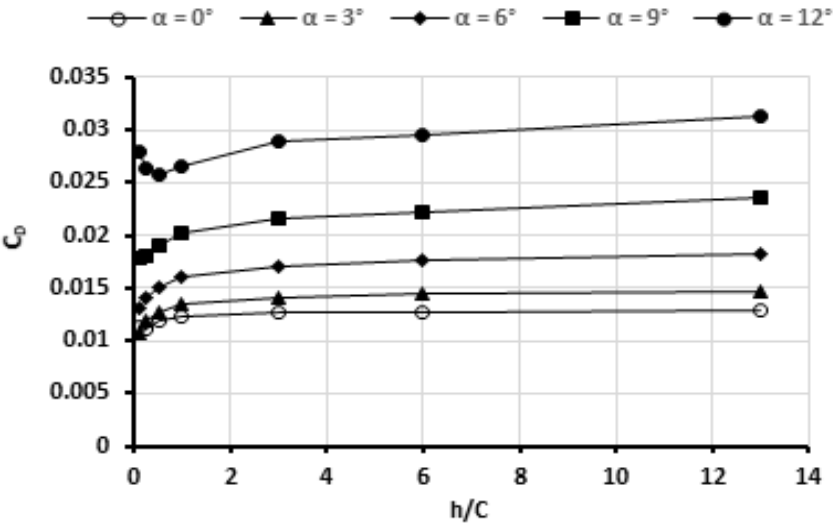


Figure 11. Drag coefficient variation with ride height at various angles of attack.

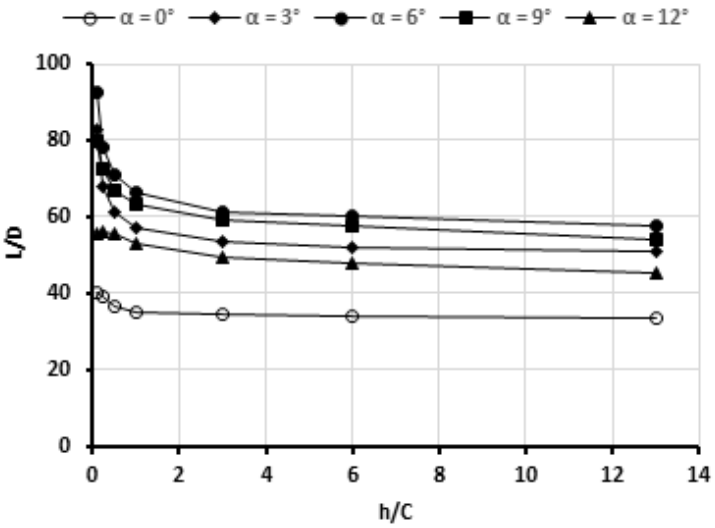


Figure 12. Lift to drag ratio variation with ride height at various angles of attack.

The ground effect on the velocity contours around the airfoil at a ride height of (h/C) = 0.1 is shown in Fig. 13. As observed, the velocity decreases along the pressure side, shifting the stagnation point further downstream on the lower surface as α increases. The onset of flow separation occurs near the trailing edge of the airfoil at α = 6.

As α increases, the separation point propagates upstream, ultimately reaching the leading edge at α = 12° and 15°, respectively. This indicates that the ground effect accelerates flow separation, causing the aerodynamic characteristics to deviate significantly from those observed in unbounded airflow conditions. Fig. 14 illustrates the steady separated flow pattern on the upper surface of the NACA 4412 airfoil near the trailing edge. At α = 15°, a separation zone forms and progresses toward the leading edge, expanding due to the intensified adverse pressure gradient. Furthermore, this separation zones become increasingly pronounced as the ride height decreases.

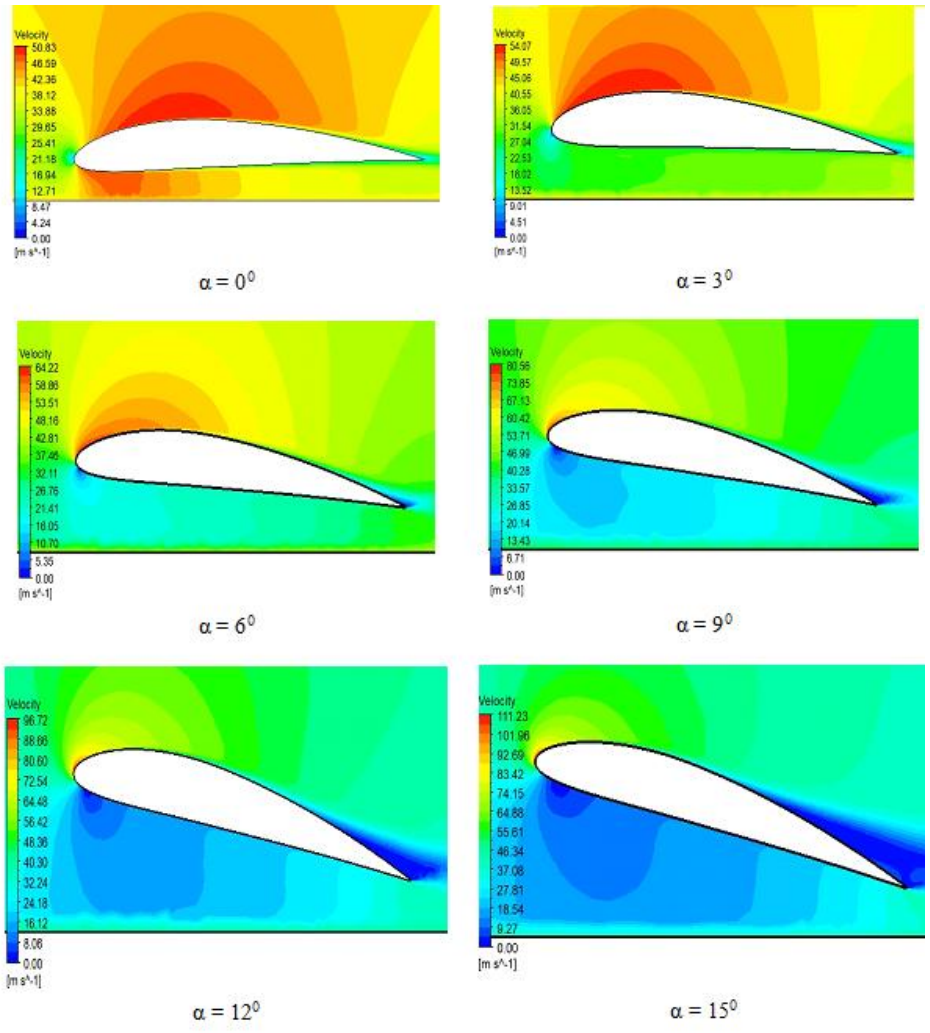


Figure 13. Velocity contours for flow at h/C = 0.1

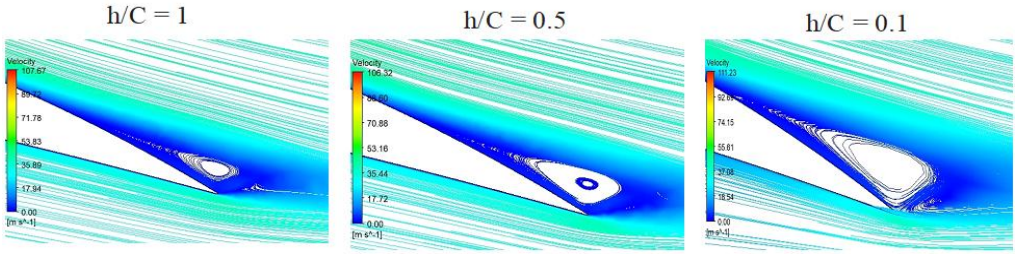


Figure 14. Stream lines and separation zones at α = 15° at various rise heights

The velocity contours around the NACA 4412 airfoil at α = 6^0 are shown in Fig. 15. The dependence of the mean flow field on (h/C) is remarkably weak; consequently, the flow patterns across different ride heights remain highly similar at this specific angle of attack. It is evident that the velocity decreases along the pressure side as the airfoil approaches the ground, indicating that the airfoil rides on a high-pressure air cushion generated above the ground surface. Furthermore, the stagnation point shifts further downstream on the lower surface as a direct consequence of the ground effect.

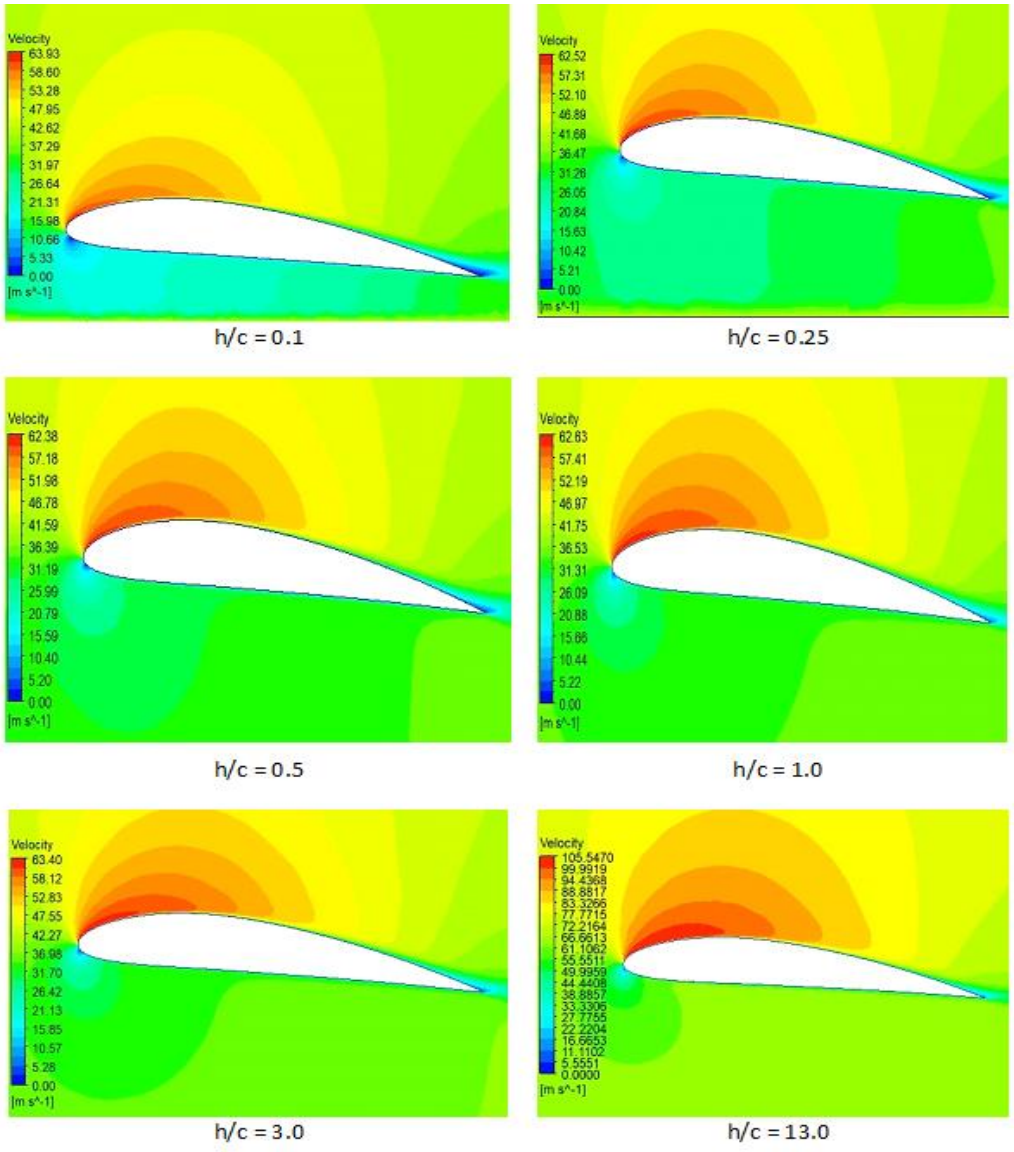


Figure 15. Velocity contours at α = 6° at various ride heights.

Figure 16 shows the variation of the mean pressure coefficient (-Cp) on the airfoil surface for four distinct angles of attack 0°, 6°, 12°, and 15° at various **(h/C)** values. For α = 0°, suction and compression effects occur near the leading edge on the lower and upper surfaces, respectively, across all ride heights. Consequently, the pressure on the upper surface is higher than that on the lower surface, meaning that the magnitude of (-Cp) on the lower surface exceeds that on the upper surface, as illustrated in Fig. 16(a). However, downstream of the leading edge region, the pressure distribution reverses, resulting in a higher pressure on the lower surface than on the upper surface. As the angle of attack increases, the distribution of (-Cp) alters significantly, particularly in the leading edge region, as shown in Figs. 16(b–d). Nevertheless, a similar qualitative trend in (-Cp) variation is maintained along the airfoil surface across the different (h/C) values.

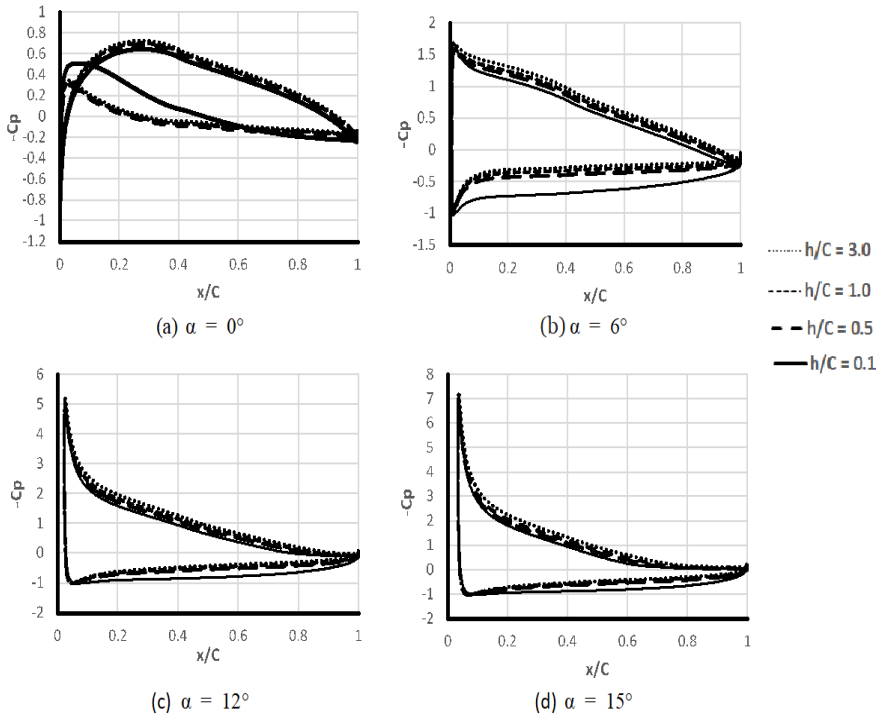


Figure 16. Pressure coefficient distributions on the NACA 4412 airfoil at various ride heights.

5. Conclusions

The present study investigated the ground proximity effect on the flow over a NACA 4412 airfoil. The Reynolds-Averaged Navier-Stokes **(**RANS**)** equations, in conjunction with the shear-stress transport **(**SST**)** k-ω turbulence model for closure, were solved using the commercial CFD package, ANSYS Fluent 2025R1. The problem was analyzed across a wide range of angles of attack (-3° ≤ α ≤ 18°) and normalized ride heights (0.1 ≤ h/C ≤ 13.0). The resulting aerodynamic characteristics; including lift, drag, pressure distributions, and velocity contours were comprehensively analysed over the tested parameters. Several salient conclusions can be drawn from this work:

1. Both the angle of attack and ground clearance exert a profound influence on the aerodynamic characteristics of the airfoil within the ground effect zone.
2. The airfoil experiences an enhancement in lift as the ride height decreases. This lift increment is primarily driven by the elevated static pressure on the low er surface (ram-air effect); however, since this is a 2D study, this behavior is independent of wingtip vortex suppression.
3. At lower angles of attack α = 9°, the drag coefficient increases slightly with increasing ride height. Conversely, at α = 12° a local maximum in CD occurs at the lowest ride height (h/C) = 0.1 due to the severe modification of the pressure distribution.

4. Beyond a specific threshold distance from the ground, the variations in C_L and C_D become negligible. Ultimately, the optimum aerodynamic efficiency with a maximum lift-to-drag (L/D) ratio of 92 is achieved at $\alpha = 6°$ and (h/C) = 0.1.
5. The results conclusively show that ground proximity exerts a significant effect on airfoil aerodynamics. Specifically, at an angle of attack $\alpha = 6^o$, reducing the ride height from 3.0C to 0.1C, results in an increase in the C_L by up to 15.7%, a decrease in the C_D by up to 17.2%, and enhancement of the (L/D) ratio by 33.8%.

6. Conflict of Interest

Authors declare that there is no conflict of interests regarding the publication of the paper.

REFERENCES

[1] Nandkumar, B.; Raksheet, C.; Potdar, S.; Yash, M.; and Khare, S. Design and analysis of wing in ground effect vehicle. Advances in Aerospace Sci. and App., 2021, Vol. 11, No. 1, pp. 11-31.

[2] Hussain, I. Y.; and Abood, M. S. Experimental study of CLARK-Y smoothed inverted wing with ground effect. Int. J. of Computer Applications, 2016, Vol. 147, No. 1, pp. 45-54. https://doi.org/10.5120/IJCA2016910962

[3] Abdizadeh, G. R.; Farokhinejad, M.; and Ghasemloo, S. Numerical investigation on the aerodynamic efficiency of bio-inspired corrugated and cambered airfoils in ground effect. Scientific Reports, 2022, No. 12:19117. https://doi.org/10.1038/s41598-022-23590-2

[4] Aananthan, M; Aravind V. G.; Tharakan, H.; and Menon, S. G. Wing in ground effect analysis using Ansys. J. of Engg. Res. and App., 2018, Vol. 8, Issue 8 (Part -III), pp. 01-06. https://doi.org/10.9790/9622-0808030106

[5] Qu, Q.; Lu, Z.; Liu, P.; and Agarwal, R. K. Numerical study of aerodynamics of a Wing-in-Ground-Effect craft. Journal of Aircraft, 2014, Vol. 51, No. 3, pp. 913-924. https://doi.org/10.2514/1.C032531

[6] Lu, A.; Tremblay-Dionne, V.; and Lee, T. Experimental study of aerodynamics and wingtip vortex of a rectangular wing in flat ground effect, Journal of Fluids Engineering, 2019, Vol. 141, No,11, 111108 . https://doi.org/10.1115/1.4043593

[7] Mehraban, A. A.; and Djavareshkian, M. H. Experimental investigation of ground effects on aerodynamics of sinusoidal leading-edge wings. Journal of Mechanical Engineering Science, 2021, Vol. 235, No, 19, pp. 3988-4001. https://doi.org/10.1177/0954406220975422

[8] Lee, T.; and Lin, G. Review of experimental investigations of wings in ground effect at low Reynolds numbers. Frontiers in Aerospace Engineering, 2022, 1, 975158 . https://doi.org/10.3389/fpace.2022.975158

[9] Almeida, O.; and Franzini, P. H. B. Experimental analysis of the flow over a wing under ground and down force effects. International Journal of Research Studies in Science, Engineering and Technology, 2023, Vol. 10, Issue 3, pp. 01-10. https://doi.org/10.22259/2349-476x.1003001

[10] Gross, J.; and Traub, W. L. Experimental and theoretical investigation of ground effect at low Reynolds numbers. Journal of Aircraft, 2012, Vol. 49, No. 2, pp. 576-586.

[11] Patek, Z.; Vrchota, P.; Jan Cervinka, J. Experimental and computational study of ground effect on airfoil section. 30th Congress of the international council of the aeronautical science, ICA2016, Daejeon, Korea, September 25-30, 2016.

[12] Traub, W. L. Experimental and analytical investigation of ground effect. Journal of Aircraft, 2015, Vol. 52, No. 1, pp. 576-586. https://doi.org/10.2514/1.C031595

[13] Doolabi, M. H.; Bakhtiarifar, M.; and Sadati, H. Experimental study of airfoil aerodynamic behavior under oscillating motion in ground effect, Journal of Applied Fluid Mechanics, 2024, Vol. 17, No. 11, pp. 2411-2423. https://doi.org/10.47176/jafm.17.11.2596

[14] Hami, K. Turbulence modeling a review for different used methods. International Journal of Heat and Technology, 2021, Vol. 39, No. 1, pp. 227– 234. https://doi.org/10.18280/ijht.390125

[15] Omer, E. A. A; Alkharboushi, A.; and Ahmed, Z. Numerical study of turbulent flow aerodynamics around a multi-element airfoil, Univ Zawia J Eng Sci Technol (UZJEST), 2025, Vol. 3, Issue 1, pp. 26-42. https://doi.org/10.26629/uzjest.2025.03

[16] Elfaghi, Abdulhafid, Ashraf Ali Omar, and Waqar Asrar. 'Higher-Order Compact-Flow Field-Dependent Variation (HOC-FDV) Method for Solving Two-Dimensional Navier-Stokes Equations'. *International Journal for Computational Methods in Engineering Science and Mechanics* 16, no. 4 (2015): 256–63. https://doi.org/10.1080/15502287.2015.1048386

[17] Menter, F. R. Two-equation eddy-viscosity turbulence models for engineering applications, AIAA Journal, 1994, Vol. 32, No. 8, pp. 1598–1605. https://doi.org/10.2514/3.12149

[18] Abugnah, E.K., Salim, W.S.I.W., Elfaghi, A.M. and Ngali, Z., 2022. Comparison of 2D and 3D modelling applied to single phase flow of nanofluid through corrugated channels. *CFD Letters*, *14*(1), pp.128-139. https://doi.org/10.37934/cfdl.14.1.128139
[19] Launder B. E.; Spalding D. B. The numerical computation of turbulent flows, Computational Methods. Appl. Mech. Eng., 1974, Vol. 3, pp. 269–289. https://doi.org/10.1016/0045-7825(74)90029-2
[20] Omer, E. A. A.; Momen, M. H.; and Yahia, N. R. Enhancement of airfoil aerodynamic characteristic by surface modification, Univ Zawia J Eng Sci Technol, 2023, Vol. 1, Issue 1, pp. 60-71. https://doi.org/10.26629/uzjest.2023.06
[21] De Fezza, G.; and Barber, S. Parameter analysis of a multi-element airfoil for application to airborne wind energy. Wind Energy. Sci., 2022, Vol. 7, pp.1627–1640. https://doi.org/10.5194/wes-7-1627-2022
[22] Barber, T. J.; Leonardi, E.; and Archer, R. D. A technical note on the appropriate CFD boundary conditions for the prediction of ground effect aerodynamics. Aeronautical Journal, 1999, Vol. 103, No. 1029, pp. 545–547. https://doi.org/10.1017/S0001924000064368
[23] Versteeg, H.; and Malalasekera, W. An Introduction to Computational Fluid Dynamics, second edition, Pearson Education Limited, Harlow, Essex CM20 2JE, England, 2007, pp. 98-110.
[24] Qu, Q.; Wang, W.; Liu, P.; and Agarwal, R. K. Airfoil aerodynamics in ground effect for wide range of angles of attack. AIAA Journal, 2015, Vol. 53, No. 4, pp. 1048 – 1060. https://doi.org/10.2514/1.J053366
[25] Abbott, I. H.; Von Doenhoff, A. E.; and Stivers, L. Jr. Summary of airfoil data, NASA TM-824, 1945.